Particle-based model for functional and diffusion layers of solid oxide cells electrodes

Hamza Moussaoui, Johan Debayle, Yann Gavet, Peter Cloetens, Jérôme Laurencin

Particle-based model for functional and diffusion layers of Solid Oxide Cells electrodes

H. Moussaoui[1], J. Debayle[2], Y. Gavet[2], P. Cloetens[3], J. Laurencin[1,*]

[1] Univ. Grenoble Alpes – CEA/LITEN, 38054, Grenoble, France

[2] École Nationale Supérieure des Mines de Saint-Etienne, SPIN, CNRS 5307, LGF, F-42023 Saint-Etienne, France

[3] European Synchrotron Radiation Facility (ESRF), 38000, Grenoble, France

Highlights

• Novel particle-based model development for Solid Oxide Cell electrodes microstructure

• Model adaption for the functional and current collecting layers

• Synthetic microstructures morphological and physical validation on 3D reconstructions

• Representativeness checked on synchrotron X-ray and FIB-SEM reconstructions

• Fine quantification of the different porosity length-scales within the substrate

Abstract. A novel particle-based model is proposed to generate synthetic yet representative 3D microstructures of typical SOC electrodes. The model steps can be related to the real electrode manufacturing routes, classically via powders processing, making it a practical tool for electrodes design optimization. The representativeness of the synthetic microstructures is checked on several two-phase (LSCF, LSC) and three-phase (Ni-YSZ) electrodes reconstructed by synchrotron X-ray and FIB-SEM tomography. The validation shows a very good agreement between the real and synthetic media in terms of metric, topological and physical properties. Furthermore, the model is adapted to simulate the microstructure of a typical Ni-YSZ current collecting layer by taking into account a bimodal pore-size-distribution. In this objective, the macro-pores resulting from the burning-off of specific pore-formers are morphologically separated in the reconstruction from the micro-porosity network. Finally, the geometrical features of the macro-pores are meticulously characterized and successfully emulated by using parametric ellipsoids.

Keyword: SOFC, SOEC, electrode modeling, microstructure, particle-based model, X-ray tomography, macroporosity.

*Corresponding author: Telephone: +33 (0) 438782210, Fax: +33 (0) 438784139,
E-mail: jerome.laurencin@cea.fr

1 Introduction

The industrial development of the renewable energy sources, such as wind turbines or solar panels, is considered as the main solution to meet the ever-growing demands and to face the exhaustion of the fossil fuel reserves. However, because of the intermittent nature of these energy sources, their utilization requires new innovative solutions to match the fluctuations between the demand and the production. A flexible energy system for storing energy is thus required to absorb the peaks of production or consumption [1]. Considering the hydrogen as the most promising energy vector, Solid Oxide Cells (SOCs) have attracted attention as an efficient and flexible electrochemical energy conversion system. Indeed, thanks their reversibility, the same object can be alternatively used to transform hydrogen into electricity (SOFC for the fuel cell mode) and *vice versa* (SOEC for the electrolysis mode) [2].

The SOCs are composed of a dense electrolyte sandwiched between two porous electrodes. The state of the art for the SOCs materials are Yttria Stabilized Zirconia (YSZ) for the electrolyte while the fuel electrode is a cermet made of Nickel and YSZ (Ni-YSZ) [2,3]. Mixed Ionic and Electronic Conductors (MIECs) such as Lanthanum Strontium Cobaltite (LSC) or Lanthanum Strontium Cobalt Ferrite (LSCF) are classically used as oxygen electrode materials. Recently, the addition in LSCF (or LSC) of a highly ionic conducting phase such as Gadolinium-Doped Ceria (GDC) has shown promising results [4,5]. Concerning the cell design, two types of geometries are usually considered based on the electrolyte or electrode supported cell. In the latter configuration, a thick porous Ni-YSZ is used as substrate on which the thin electrodes and electrolyte are layered.

The selection of raw materials with high electronic and/or ionic conductivity, high activity for the reactions and low reactivity with other components is certainly crucial for the performances and durability of SOCs. Nevertheless, the effective properties of the porous electrodes can largely differ from the intrinsic characteristics of the dense materials [6,7]. For this reason, the charge and mass transfer as well as the effective electrochemical activity within the electrodes are strongly dependent of the morphological characteristics of the microstructure [4,8-11]. Regarding the Ni-YSZ support, the gas diffusion losses across the thick layer, which can affect the cell

response when operated at high current density, are also highly sensitive to the porosity network [12-14]. Therefore, the complex microstructures of both the electrodes and the Ni-YSZ substrate have a huge impact on the cell performances. Besides, it is also known that the electrode microstructure plays a key role on the cell durability. For example, a coarse cermet microstructure for the H_2 electrode favors the Ni depletion under electrolysis operation while a fine microstructure allows limiting this issue [15-17]. Moreover, the porosity level and the Ni/YSZ ratio can affect the cermet long-term stability as well [17]. For all these reasons, the microstructure of both the electrode and the cell support can be optimized to improve the cell performances and durability.

In this objective, it is crucial to characterize the morphological details of the microstructure by keeping a large field of view for the observations. This latter requirement is necessary to capture all the heterogeneities distributed within the porous media. In this frame, the recent developments of 3D imaging techniques have been successfully applied to reconstruct the SOCs electrodes microstructure. The technique based on the Focused Ion Beam sectioning coupled with a Scanning Electron Microscope (FIB-SEM) is especially well adapted for the SOCs electrodes [18-20]. Indeed, it allows resolving fine details of few tens of nanometers with reconstructed volumes of 10^3-20^3 μm^3. In complementarity with the FIB-SEM method, synchrotron X-ray absorption tomography [21-23], ptychography [24-26] or holotomography [11,27-29] have also been successfully employed to reconstruct samples with a high spatial resolution. In the latter case, reconstructions with a field of view as large as 50^3 μm^3 have been obtained [27, 29-31]. This feature is essential to obtain good statistics of the heterogeneous microstructure especially for the cell support for which the Representative Volume Element (RVE) is in the order of 35x35x35 μm^3 [28]. This large RVE is mainly due to the presence of large pores in addition to the micro-porosity network resulting from partial powders sintering and the NiO reduction. Therefore, from our best knowledge, only one reconstruction of the Ni-YSZ support has been published [29].

The electrode microstructural optimization is a time-consuming task, as it requires the manufacturing and the characterization of many samples [20,32]. Therefore, a modeling approach based on the generation of synthetic microstructures can be helpful by providing recommendations and guidelines with the identification of targeted

electrode properties. Moreover, the synthetic microstructures can be used to derive the mathematical correlations linking some key properties such as the density of Triple Phase Boundary lines (TPBls) to the geometrical attributes of the electrode (composition, porosity and particle size distribution of the solid phases) [33-35]. Therefore, many attempts have been devoted to the development of relevant 3D geometrical models able to mimic the actual microstructure of SOCs electrodes. Nevertheless, despite its crucial importance regarding the cell performances and robustness, there is still no available model developed for the specific microstructure of the Ni-YSZ exhibiting a bi-modal pore size distribution.

Two kinds of models can be distinguished according to whether they adopt a pure mathematical approach based stochastic geometry or they involve a particle-based process. The former methods present the advantage of very fast executing time since they are not based on iterative processes. Besides, it has been shown that they can produce synthetic microstructures that mimic accurately the SOCs electrodes. For example, Moussaoui et al. [31] have adapted the multigaussian random fields to emulate representative two-phase and three-phase electrodes. Neumann et al. [36] have also proposed a model based on beta-skeletons providing relevant synthetic microstructures. The major drawback of these pure mathematical approaches is that it is difficult to link the synthetic microstructure to the electrode manufacturing based on the sintering of powders (with techniques such as the tape-casting or the screen-printing).

Conversely, the particle-based models present the advantage to be more easily related to the electrode manufacturing. Indeed, the particle collection used for the simulations can be linked to the powders employed in the electrode manufacturing [37,38]. However, these models, which are based on iterative algorithms, require longer executing time to generate the synthetic microstructures. Besides, their geometrical representativeness can be questionable if compared to the real SOC electrode microstructure in which the phases exhibit a complex and continuous shape [39]. Indeed, as a general matter, the final synthetic microstructure keeps the reminiscence of the initial particles geometry used for the packing. For example, Choi et al. [40] have compared a FIB-SEM reconstruction to a numerical microstructure generated by sphere packing. They obtained significant differences in the resulting structures.

Consequently, Neumann et al. [36] have mentioned that these approaches must allow qualitative conclusions even if 'their applicability to real materials are still unclear'. From this point of view, a particle-based model producing representative synthetic microstructures of real electrodes is still missing.

A detailed description of the particle-based methods is already available in [31,41,42] so that only a brief review is given hereafter. In general, these methods are based on a random packing of spheres [39,43] with a uniform particle size whereas only few studies consider a more realistic distribution on the spheres radii [37,44]. The numerical procedures begin by distributing initial spheres or "seeds" in the domain. This first step is generally done by the so-called "drop & roll" algorithm [10,44-46] or by the random positioning of "seeds" on a lattice structure [41,43,47]. This step is crucial as it can lead to irrelevant structuration or anisotropy in the final microstructure [48-50]. Then, the medium is densified according to different methods such as the expansion of the initial spheres [41,46,48,49], the overlap of spheres [10,44,45], or the creation of necks [47].

In this study, an original particle-based algorithm is proposed to generate synthetic microstructures. A special attention has been paid to add specific constrains in the model in such a way that it can yield synthetic microstructures representative of real SOCs electrodes. The model ability to mimic real microstructures has been checked on various LSCF, LSC and Ni-YSZ electrodes reconstructions. Moreover, the model has been built to be flexible with the possibility to emulate different kinds of electrodes microstructures. In particular and for the first time, the microstructure of the Ni-YSZ substrate with a bimodal pore size distribution has been simulated with an adapted version of the model. The relevance of the synthetic microstructure has been also verified thanks to a specific reconstruction obtained by synchrotron X-ray holotomography. The present article is organized as follows. First, the experimental part of electrode reconstruction and characterization is presented in Section 2. The model description is given in Section 3, while its validation is summarized in Section 4. Finally, the model flexibility to emulate the Ni-YSZ support is illustrated in Section 5.

2 Experimental: three-dimensional electrode reconstruction and characterization

2.1 Cells and materials

Two different complete cells were analyzed in the frame of this work. Both are commercial circular cells with the H_2 electrode used as mechanical support. The first investigated cell, later named Cell-A, consists of a dense 8%mol Yttria Stabilized Zirconia (YSZ) electrolyte of 5 µm supported by a 260 µm thick porous Ni-YSZ cermet (used as H_2 electrode). The active part of the O_2 electrode is a porous bilayer composed of a LSCF-GDC composite (15 µm) associated with a LSCF inlayer (18 µm) on which is deposited a current collector in LSC (20 µm). A thin barrier layer of GDC is also added between the electrolyte and the O_2 electrode (~ 3 µm) in order to limit the chemical reactivity between LSCF and YSZ.

The second cell, referenced as Cell-B in the following of the article, presents a Ni-YSZ H_2 electrode as well, composed of a thick current collector (500 µm) co-sintered with a thin active functional layer (10 µm). The cermet bilayer is used as structural support on which is layered the YSZ electrolyte (5 µm), the thin GDC barrier layer (2 µm) and the O_2 electrode in LSC (40 µm). The H_2 electrode and the electrolyte were manufactured by water-based tape casting and co-sintered, while the barrier layer and the O_2 electrode were applied on the electrolyte by screen printing.

A polished cross section of this cell was observed by Scanning Electron Microscopy (SEM) using the Back-Scattering Electron (BSE) mode (Philips XL30). The acquired micrograph is shown in Fig. 1 with the porosity in black and the solid phases in grey. It is worth noting that the substrate is characterized by the presence of large disconnected pores with a typical size in the range of few micrometers in addition to a fine network of micro-porosities. SEM images acquired at higher magnification show the other constitutive cell layers (Fig. 1).

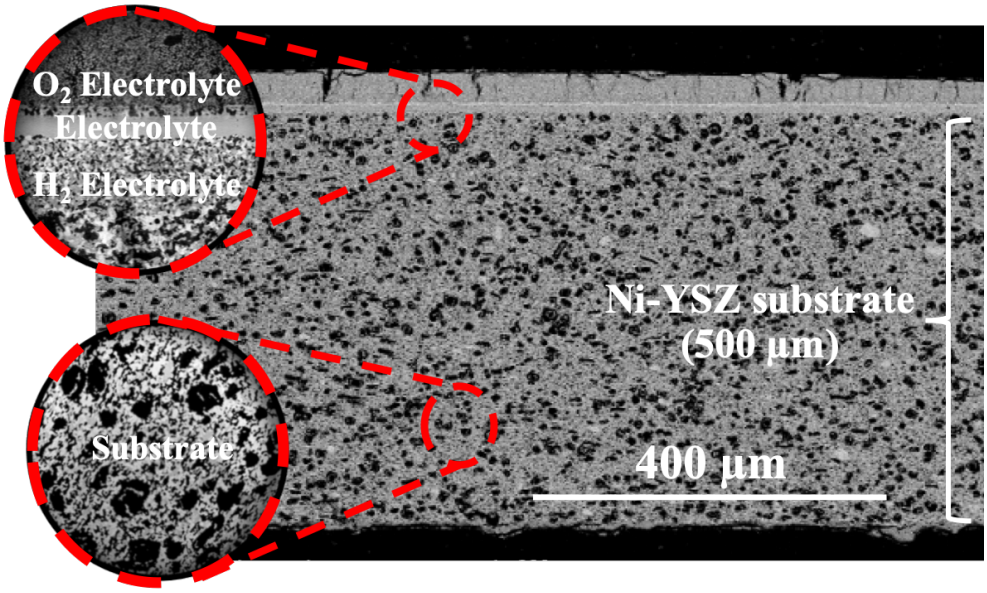

Fig. 1. SEM cross-section image of Cell-B observed in EsB mode. Higher magnification images reveal the different constitutive cell layers (black color representing porosity, dark grey Ni, and bright grey YSZ).

2.2 3D reconstructions by synchrotron X-ray nano-holotomography and FIB-SEM

Two techniques were used in the frame of this study to obtain the reconstructions of the investigated electrodes microstructures, the FIB-SEM tomography and X-ray holotomography. The choice of the method to use depends on the targeted volume size and resolution. As a general matter, FIB-SEM is well adapted to reconstruct electrodes with a fine microstructure (such as the electrode functional layer for example), for which high image resolution and intermediate reconstructed volume are needed. Indeed, as already mentioned, this method allows imaging microstructures with a very fine spatial resolution of down to 10 nm (with reconstructed volumes of around 10^3-20^3 μm^3 size). In contrast, the synchrotron X-ray holotomography is well adapted for specific microstructures requiring higher volume by keeping a good resolution in order to characterize large and fine morphological features in the same reconstruction [11,30,51].

Therefore, depending on the targeted resolution and volume size, one of the two methods has been adopted. In practice, as it exhibits a very fine microstructure, only

the O_2 electrode of Cell-B was reconstructed by FIB-SEM tomography using a cubic voxel size of 16 nm. The imaging of the substrate of Cell-B and the rest of the electrodes was carried out by synchrotron X-ray holotomography at the beam line ID16A at ESRF (European Synchrotron Radiation Facilities). In this case, the reconstructions were acquired with a cubic voxel size of 25 nm (corresponding to a physical spatial resolution estimated to 50 nm [11,30]). The description of the protocol for the FIB-SEM acquisition is already detailed in [4,31] while the one for the holotomogphy experiments and reconstruction is extensively presented in [11,15,30]. It is worth noting that the electrode reconstructions for the functional layers have been already presented in [31] while the electrode reconstruction for the current collector of Cell-B has been specifically acquired for the present study.

2.3 Image analysis for microstructural characterization

In order to obtain the final 3D microstructures, the raw images in grey-scale level have been pre-processed and segmented according to the methods detailed in [52,29]. The microstructural properties in terms metrics and topological parameters were then computed thanks to a set of numerical tools already presented and thoroughly detailed in [53,31]. In this study, the volume fraction (ε), the connectivity (δ), the mean phase diameter (d_p) the geometrical tortuosity factor (τ^{geo}) (centroid path method [54]), the constrictivity parameter (β), the specific surface area (S_p), the density of TPBls (ξ_{TPBls}) and the M-factor (ratio between the effective and intrinsic conductivities or diffusivities) were systematically calculated for all the reconstructions. The determination of these morphological parameters was complemented by the computation of the Particle Size Distributions (PSDs) and the covariance functions [31].

Furthermore, a special attention has been paid in this study to analyze the microstructure of the Ni-YSZ support of Cell-B exhibiting a bimodal pore size distribution (Fig. 1). Indeed, the identification and then the separation of the macropores resulting from the burning-off of specific pore-formers from the microporosity network (arising from the incomplete electrode densification and NiO reduction) is a crucial step in order to characterize the two radically different morphologies, and therefore investigate the properties of each porosity length-scale. As

both types of porosities are identified with the same label in the segmented reconstruction, a specific procedure based on mathematical morphology [55] has been developed. The methods to separate the macrospores from the rest of the volume is divided in three subsequent steps illustrated in Fig. 2 and summarized hereafter:

(1) The method starts by applying a morphological erosion on the total pore phase. For this purpose, a small spherical structuring element is used to remove the very small porosities in the volume. This operation leads to shrink the pore phase according to the radius of the structural sphere. As a result, the initial percolated network of micro-pores is deleted in part yielding to a set of disconnected micro and macro pores.

(2) The second step consists in removing the small-disconnected porosities from the reconstruction. For this purpose, each of the disconnected pores are labeled and then removed if their size is smaller than a critical value.

(3) Finally, a morphological dilatation is applied on the pore phase using a spherical structuring element of the same size of step *(1)*. This operation allows retrieving the initial external frontier of the macropores that was moved inward by the initial morphological erosion of step *(1)*.

Fig. 2. Illustration of the different steps for the separation of the macropores from the micropores network. Step *(2)* was not necessary in this particular illustrative case, as the fine micropores were deleted using step *(1)*.

3 Model description

A flexible model based on the packing of spherical spheres has been developed in the frame of this study in an attempt to emulate representative two-phase and three-phase electrode microstructures. For this purpose, the model has been built with specific constraints to control the heterogeneity of the microstructure and its morphology.

3.1 Two-phase material for O_2 electrode

In order to generate two-phase synthetic microstructures representative of the O_2 electrode, the model has been divided into a sequence of three steps detailed hereafter:

(a) Initial sphere allocation – The microstructure generation starts with an empty volume *V* in which are positioned some initial spheres with a given particle size distribution. The choice of this distribution is of capital importance to control the geometrical characteristics of the final microstructure. In practice, different distributions were tested and it was found that the Weibull function is the best compromise to reproduce the SOC electrode microstructures (Eq. 1):

$$f_{Weibull}(r;\lambda,k) = \frac{k}{\lambda}\left(\frac{r}{\lambda}\right)^{k-1} e^{-\left(r/\lambda\right)} \quad (1)$$

where *r* is the random variable for the sphere radius, and *k* and λ are respectively the shape and scale parameters of the distribution. The characteristics of the spheres population (mean, standard deviation, skewness, etc.) are expressed directly as a function of these two parameters. It is worth noting that the Weibull distribution is consistent with the one of the classical powder particles used for the electrode manufacturing. Indeed, the real powders distribution usually follows a non-symmetrical repartition [56,30], which is well captured by the Weibull function.

The positioning of the initial spheres in the domain is also crucial to control the final pattern of the microstructure and the possibility to have some local aggregation in the synthetic medium. For this purpose, a specific procedure has been implemented by dividing the domain V into n_{seed}^3 cubic sub-volumes $U_{i\in[\![1,n_{seed}^3]\!]}$. In each sub-volume,

an initial sphere is randomly placed as illustrated for a 2D slice cross-section in Fig. 3a. The number of initial spheres or seeds, $n_{seed,}$ is then a model parameter that needs to be adapted depending on the microstructure to emulate. An initial domain division in a large number of sub-volumes yields a homogeneous microstructure whereas a low number of initial spheres results in the creation of aggregates. This dependency of the microstructure homogeneity with the number of seeds is explained since any new sphere added in the generation process (cf. next step) needs to be put in contact with an existing sphere already present in the volume (in order to achieve a good connectivity in the final microstructure). In this condition, the division of the domain in sub-volumes associated to a number of seeds enables to control the level of clustering in the final microstructure.

(b) Volume filling – In order to fill the volume and reach the targeted pore volume fraction, new spheres are added in the domain in an iterative process. Assuming that they are also related to the powder particles used for the electrode fabrication, the diameters of the new spheres follow the same Weibull distribution than the initial one. As previously mentioned, each sphere is added in the domain to be in contact with an existing one, already positioned in the volume. This constraint ensures a good solid phase connectivity as it is generally observed in real microstructures [42,57]. In order to take into account the partially densified nature of the SOC electrodes, some conditions of the particle interaction/contact have to be fulfilled and are described hereafter.

Firstly, a controlled overlap is allowed between particles during the volume filling process. In practice, the distance between two overlapping spheres S_i and S_j with respective radii r_i and r_j (cf. Fig. 3e) is defined as follows:

$$d_{ij} = \frac{r_i + r_j}{2}(1 + rand^{n_{overlap}}) \quad (2)$$

where *rand* denotes a uniformly distributed random variable in the interval $[0,1]$, and $n_{overlap}$ a variable controlling the overlap distribution. In fact, values higher than unity for this paramater ($n_{overlap}>1$) lead to high degrees of spheres interpenetration while lower values ($n_{overlap}<1$) lead to more punctual contacts. A sensitivity analysis has been

conducted over this parameter, and a value of $n_{overlap}$ =1 was retained as the best compromise. This choice means that the overlap extend is equally distributed between the two bounded positions (i.e. between the maximum overlap $d_{ij} = (r_i + r_j)/2$ and the punctual contact $d_{ij} = (r_i + r_j)$).

Secondly, the direction of each new sphere with respects to the old one needs to be totally random in order to account for the isotropy of the sintered electrode. Therefore, the azimuth and elevation angles, Φ and θ, have been expressed in the spherical coordinates system as follows:

$$\Phi = 2 * \pi * rand_1 \quad \text{and} \quad \theta = \arcsin(rand_2) \tag{3}$$

Where $rand_1$ and $rand_2$ are two uniformly distributed random variables in the interval $[0,1]$. It can be noticed that the elevation angle θ is not expressed directly as a function of the random variable, but through the inverse sine function. The reason behind this choice is to avoid a privileged position close to the poles and thus to obtain uniformly distributed directions [58].

Finally, the number of interconnections is constrained in the model. Indeed, the coordination number is computed for each sphere, and a maximum value n_{coord} is set to avoid non-realistic local heterogeneities. In practice, before counting the number of coordination, it is necessary to test if two spheres are overlapping or not. This preliminary step is carried out by checking the following condition (Eq. 4):

$$\sqrt[2]{(c_{j,x} - c_{i,x})^2 + (c_{j,y} - c_{i,y})^2 + (c_{j,z} - c_{i,z})^2} \leq (r_i + r_j) \tag{4}$$

Where $(c_{i,x},c_{i,y},c_{i,z})$ and $(c_{j,x},c_{j,y},c_{j,z})$ are the Cartesian coordinates of the spheres *i* and *j* centers.

The iterative process for the volume filling is ended when the targeted volume fraction is reached. However, for time machine optimization, the phase volume fraction ε_p is not computed at each step of the simulation at the beginning of the procedure, but only when n_{opti} ~ 500 spheres are added within the domain. Then the frequency of volume

fraction, assessment is increased continuously when the simulation gets closer to the targeted value.

(c) Creation of neck curvature between sintered particles – The sintering leads to the formation of necks between the particles, which has been taken into account in the previous step of the algorithm (i.e. thanks to the volume filling by the sphere overlap). Nevertheless, the mass transfer resulting from the diffusion toward the particles intersections also yields the creation of neck curvature as illustrated in Fig. 3c. For instance, Metcalfe et al. [47] have proposed to set the radius of this neck curvature to one-twentieth of the particle diameter based on SEM observations of SOC electrodes. In our case, this radius is created by applying a morphological opening defined as the dilation of the erosion of the microstructure [55]. For this operation, a spherical structuring element has been employed. The diameter of the sphere, which is one of the model parameters, is of central importance to control the geometry of the curvature. In practice, a diameter of one-sixth to one-fifth of the mean particle diameter provides good results for typical SOC electrodes. It can also be noticed that the morphological opening induces a slight change of the electrode phase volume fractions, which is taken into account in the algorithm.

Finally, it should be mentioned that an edge effect has been observed on the resulting synthetic microstructures. Indeed, the spheres have less probability to occupy the regions close to the external faces of the simulated domain. Therefore, slices with a thickness of around a phase mean diameter has been removed from the volume sides as shown in Fig. 3d. This edge effect could be avoided as well by considering a simulation volume larger than the actual observation window [59].

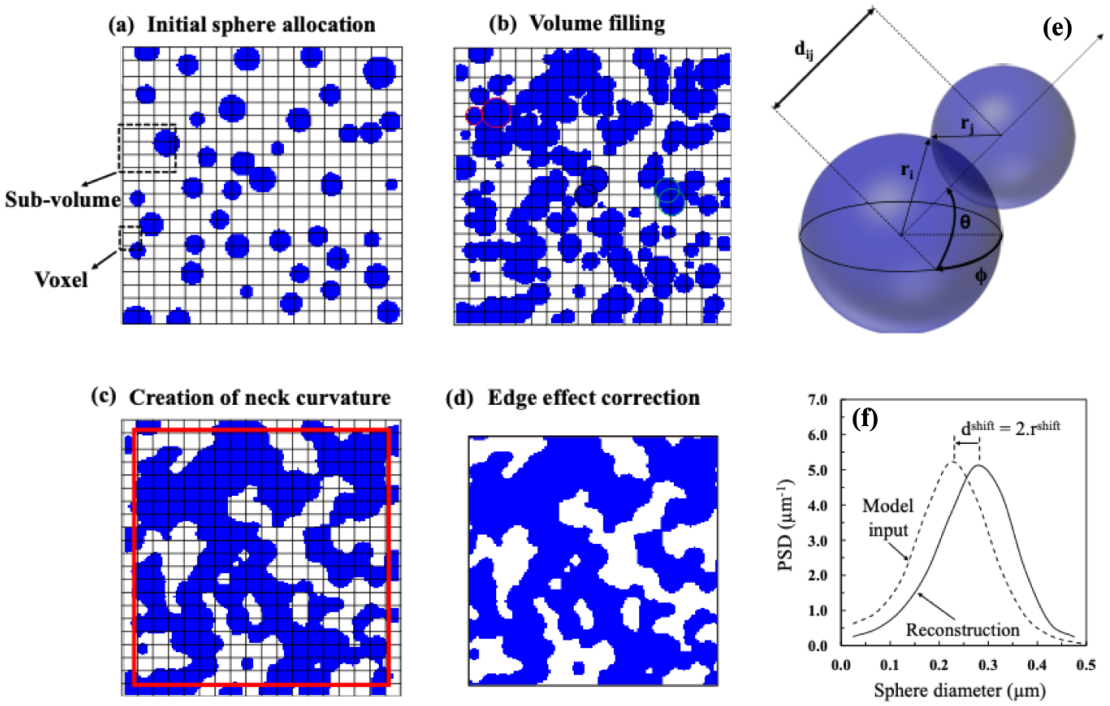

Fig. 3. (a-d) 2D illustration of the three steps for building the particle-based two-phase microstructure; (a) Initial spheres allocation, (b) volume filling (with three examples of spheres overlap extend: high, medium and low in green, black and red respectively), (c) creation of neck curvature, and (d) edge effect correction by volume cropping. (For interpretation of the references to colors in this figure legend, the reader is referred to the web version of the article.) (e) Schematic representation of the contact geometry between two particles *i* and *j* in the spherical coordinate system. (f) Illustration of the shift between the model input spheres size distribution and the reconstruction PSD for the LSCF O_2 electrode of Cell-A.

3.2 Three-phase material for H_2 electrode

The particle-based model has been extended to simulate the Ni-YSZ porous composite electrodes. For this purpose, two kinds of sphere populations related to the two electrode solid phases are used to generate the synthetic microstructure. For each case, the particles are assumed to follow a distinct Weibull distribution. The initial sphere positioning is carried out in order to respect the volume fraction of the solid phases. Then, the ionic and electronic particles networks are built step-by-step to fill the volume. In this iterative procedure, the addition of a new sphere in the domain follows the same rules than the ones defined for the two-phase electrode. However, at each step of the process, the attribution of the ionic or electronic nature of the new particle is

carried out with a constraint added to fulfill the targeted electrode composition. Besides, in order to maintain a high phase connectivity, each new sphere is positioned in contact with an existing particle of the same nature. The neck curvature between the spherical particles of the microstructure is subsequently created by applying a morphological opening for the two solid phases. For this last operation, the same structuring element has been considered for the two phases. Finally, to remove the edge effect, the thickness of the slices (which are removed from the simulated microstructure) is set to the highest mean diameter of the ionic or electronic spheres.

3.3 Model input parameters

As a general matter, the simulation of the electrode microstructure requires as input data (i) the phase volume fractions, (ii) the size of the structuring element for the morphological opening and (iii) the parameters of the Weibull distributions for the ionic and electronic conducting spheres. As already discussed, these last parameters could be roughly ascribed to the ones describing the particles size distribution for the powders used for cell manufacturing. Moreover, if the sintering is not too high, the geometrical characteristics of the particles used for the simulation should not be too far from the phase size measured on the 3D reconstruction. Therefore, these last distributions for the ionic and electronic conducting phase could be taken for the simulation. However, it has been observed that the numerical sintering leads to a linear shift between the distribution of the particles used for the simulation and the one measured on the 3D reconstruction. Thus, the input sphere size distribution needs to be shifted to accurately reproduce the microstructure according to Eq. 5 (cf. Fig. 3f):

$$\left.\frac{\mathrm{dP}}{dr}\right|^{model\ input}(r) = \left.\frac{\mathrm{dP}}{dr}\right|^{Reconstruction}\left(r + r^{shift}\right) \quad (5)$$

Where P is the cumulative probability density function of the particles radii (probability that a random sphere radius is less or equal to r), r is the sphere radius, and r^{shift} is the translation value between the input spheres PSD and the targeted reconstruction PSD (as illustrated in Fig. 3f).

For the model validation presented in the following section, the distributions of the solid phases have thus been measured on the 3D reconstructions and then shifted with a value equal to 20% of the mean radius measured on the 3D volumes. It is worth noting that this translation has been found to be the optimum shift to reproduce correctly all the tested microstructures (cf. model validation). This systematic observation suggests that there is a simple relation (given by eq. (5)), between the PSD of the final synthetic microstructures (representative of the real electrodes) and the one used for the initial spheres population. This behavior can be justified since, as mentioned in [37], the particle size and distribution of the initial powder must roughly represent the size and distribution of the particle in a sintered electrode. According to the present analysis, the relation between the two PSDs seems to be a simple shift.

4 Results

4.1 Reconstructions and microstructural characterization

4.1.1 Active layer of Cell-A and Cell-B

Microstructure visualizations and RVE estimations – The 3D rendering volumes after segmentation for the O_2 and H_2 electrodes of both cells are displayed in Fig. 6. These volumes can be used to determine the microstructural properties for all the studied electrodes. For this numerical analysis, an appropriate spatial resolution for the analyzed volume is required to catch all the microstructural details of different length-scales without leading to excessive computational time. For example, 10-15 voxels are necessary on the particle diameter to determine accurately the specific surface area [52,60]. For this reason, all the properties have been determined by keeping a voxel size of 25 nm (and 16 nm for the O_2 electrode of Cell-B) as this dimension is requested to describe precisely the fine porosity network of the electrodes (cf. results in Table1 and 2). Besides, a relevant size for the volume is also necessary to be statistically representative of the heterogeneous medium without leading to superfluous computational time as well. In this perspective, the Representative Volume Element (RVE) has been estimated for the different microstructures by using the expansion method described by Yan et al. [58]. This analysis, which is reported in the

supplementary S1, has been carried out for the M-factor. Indeed, compared to the other properties, the RVE determination for this parameter leads to the most restrictive condition requesting a large volume to obtain good statistics (the M-factor includes the effects of the volume fraction, the geometrical tortuosity and the constrictivity [7]). A typical RVE of $\approx 15^3 = 3375$ μm^3 has been determined for the H_2 electrodes functional layer while the description of the coarse microstructure for Ni-YSZ support requires a larger volume of $\approx 36^3 = 46656$ μm^3. Since the H_2 electrode active layer of Cell-B has a thickness limited to 10 μm, the computation of its microstructural properties has been carried out by averaging the data computed on 16 independent Stochastic Volume Elements (SVEs) of $\approx 8.5^3 = 614$ μm^3 (for which the standard deviation becomes negligible). Finally, the RVE for the O_2 electrodes is limited to $\approx 9^3 = 729$ μm^3 since the microstructure is only composed of one single solid-phase.

Microstructure properties determination – The microstructure properties for the O_2 and H_2 electrodes of both cells are listed in Tables 1-3. As a general matter, it is worth mentioning that the microstructural properties for the two studied cells drop within typical values for the SOCs Ni-YSZ, LSCF or LSC electrodes [61]. Nevertheless, it can be noticed that the electrodes microstructure of cell-B is substantially finer than the one of cell-A. For example, the LSCF mean phase diameter of Cell-A is almost 3/2 times the one of the LSC particles for Cell-B. Meantime, a factor of 2.16 on the mean pore size is found between the two electrodes (Table 1). Therefore, the specific surface area is much higher for the O_2 electrode of Cell-B. Regarding the Ni-YSZ cermet, the difference of microstructural properties between the two cells is less pronounced even if the coarser microstructure of Cell-A yields a lower density of TPBls (Table 2 and 3). It can be thus concluded that the electrodes of the two studied cells present typical but distinct microstructures that will be used to validate the particle-based model.

4.1.2 Current collector of Cell-B

Microstructure visualizations with macro-pores separation – The rendering volume for the reconstruction of the thick current collector of Cell-B is displayed in Fig. 4a. A set of large disconnected macropores resulting from the use of pore-formers during the manufacturing is observed in the microstructure. These macropores allow reducing the gas diffusion losses across the thick substrate. By applying the numerical procedure

detailed in Section 2.3, the macrospores have been morphologically separated from the rest of the microstructure. The visual results of this operation are shown in Fig. 4a with a volume containing only the macropores. Their close examinations reveal that they have an ellipsoid-like shape, with a variable degree of flattening going from an almost spherical to an oblate geometry. It can also be noticed that they seem homogenously distributed within this diffusion layer and they are fully disconnected from each other.

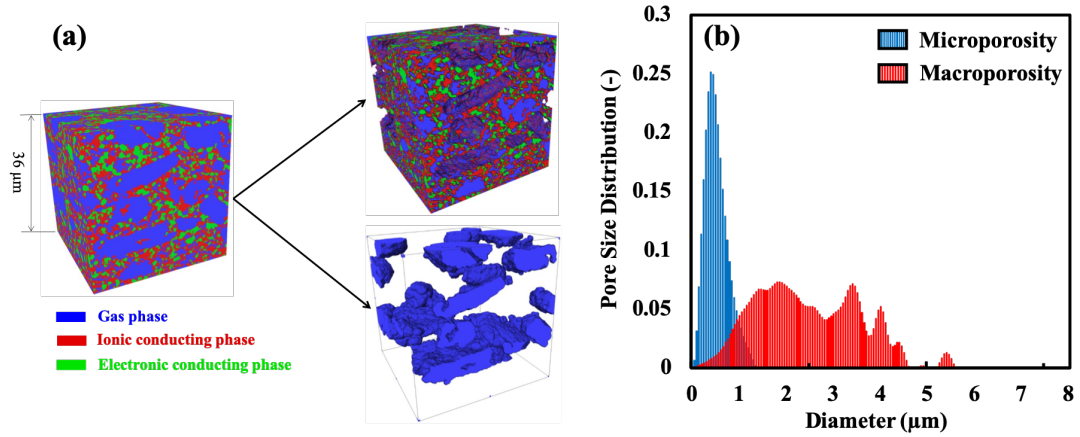

Fig. 4. (a) Illustration of the macropores separation for the current collector of Cell-B, (b) Pore Size Distribution (PSD) separated in microporosity PSD in blue and macroporosity PSD in red.

Microstructure properties determination – Taking advantage of the large reconstruction obtained by synchrotron X-ray holotomography, the microstructural properties of the current collector have been computed with a good level of confidence. The calculated properties are listed in Table 4 and are carefully analyzed hereafter.

As expected, it is found that the current collector of Cell-B exhibits a highly porous and coarse microstructure compared to the Ni-YSZ functional layer. Indeed, the pore volume fraction reaches 45.46% for the substrate while the mean YSZ and Ni diameters are respectively equal to 0.56 µm and 0.42 µm (compared to ≈ 0.3 µm for the functional layer). This statement is consistent with the rather low specific surface areas measured for the two solid phases (Sp_{YSZ} = 1.79 µm^{-1} and Sp_{Ni} = 1.25 µm^{-1}) that are almost two times lower with respect to the ones in the active layer. It can be noticed that a higher content of Ni is found in the solid phase $\varepsilon_{Ni}/(\varepsilon_{YSZ}+\varepsilon_{Ni})$ = 36.10%, compared to 32.75% for the functional layer. Indeed, a higher Ni proportion is needed in the current

collecting layer to ensure a good electronic conductivity and electrical contact with the interconnects. Besides, all the phases are well connected as the different volume fractions do not drop below the percolation threshold. Moreover, both solid phases are more tortuous and constrictive leading to lower conductivities compared to the functional layer (M_{YSZ} = 0.100, M_{Ni} = 0.011). Finally, it can be noticed that the coarse microstructure of the current collector results in a low density of connected TPBls of 3.19 μm^{-2}.

Impact of macro-pores on the gas phase properties – Thanks to the macro-porosity identification, the morphological characteristics of the macro- and micro-pores can be evaluated independently. The properties calculated for the two types of pores are also reported in Table 4. It can be seen that the volume fraction of macrospores (14.21%) increases significantly the total porosity of the support whereas the one for the micro-porosity network remains comparable to the functional layer. Besides, the disconnected macro-pores identification allows separating the contribution of each porosity length-scale to the whole porosity bimodal distribution. The result is shown in Fig. 4b where the particle size distribution is plotted for the two types of porosities. Thanks to this analysis, a mean diameter of 0.61 µm was found for the micro-porosity network, whereas the larger-scale porosities exhibit a mean size of 2.48 µm. The macro-pore size distribution reveals a relatively high standard deviation of $\sigma = 1.18\ \mu m$ and a positive skewness of γ = 0.50. The difference in pore size and volume fraction between the two porosity length scales leads to a pronounced unbalance between the specific surface area developed by the microporosity $Sp_{micropore}$ = 1.92 μm^{-1}, and the one by the macro-porosity $Sp_{macropore}$ = 0.28 μm^{-1}. As expected for a highly porous layer, the gas paths are less tortuous compared to the functional layer, with $\tau_{Pore}^{geo} = 1.62$. However, because of the large bimodal pore size distribution (Fig. 4b), a large difference was obtained between the maximum section S_{max}, dominated by the macro-porosity and the necks size S_{min} controlled by the micro-porosity. This leads to a pronounced bottle-neck effect quantified to $\beta_{Pore} = 0.20$.

It is worth reminding that the macro-pore size distribution (Fig. 4b) can be related to the employed pore-formers distribution as their morphology is quite conserved after sintering in the final microstructure [62]. Concerning the orientation, it can be observed from Fig. 4a that the macropores are almost perpendicular to the vertical axis and thus

parallel to the electrode/electrolyte plane. To quantify this statement, each volume was fitted with an ellipsoid geometry as illustrated in Fig. 5a. This allowed obtaining an approximation of the distribution of these voids dimensions and orientation [63]. It was found that the volumes have a mean tilt angle of ~ 6°, while no privileged orientation has been detected within the parallel plane to the electrode (xy-plane). To quantify the impact of this orientation on the mass transfer, the ratio between the intrinsic and effective gas diffusivity (M-factor) was calculated. As expected, a noticeable difference was found between the three space directions. Indeed, a very close M-factor was obtained in the two parallel directions to the electrode surface $M_{Pore}^{x} \approx M_{Pore}^{y} = 0.156$, while a lower diffusivity was obtained in the orthogonal direction to the electrode $M_{Pore}^{z} = 0.100$. This anisotropy is obviously related to the privileged macropores orientation reported before. This trend was also observed for the YSZ and Ni phases ($M_{YSZ}^{x,y} = 0.112; M_{YSZ}^{z} = 0.083$ and $M_{Ni}^{x,y} = 0.012; M_{Ni}^{z} = 0.009$). This tendency is opposed to the desired cell characteristics, as the transport phenomena in the support are supposed to be favored in the orthogonal direction to the electrode (i.e. z-direction). This anisotropy of the substrate could be related to its manufacturing method by tape casting [64] that induces a privileged orientation as discussed in [65]. Therefore, the present study based on the detailed morphological analysis of a large 3D reconstruction reveals that the macro-pores in the cell could still be optimized to improve the gas diffusion.

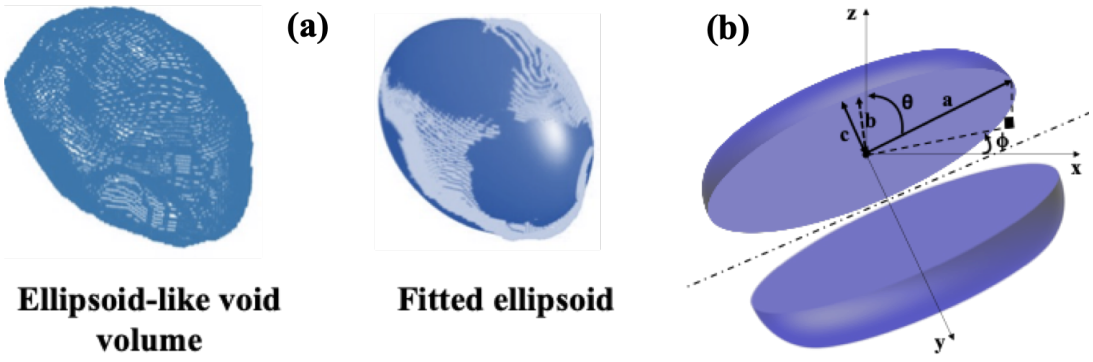

Fig. 5. (a) Illustration of a macropore volume fitting to an ellipsoid. (b) Schematic representation of an ellipsoid cut used in the macropores simulation. An illustration is given for the three space lengths a, b and c in a spherical coordinates system where θ is the polar angle (tilt angle with respects to z-axis) and ϕ is the azimuth angle (rotation within the xy-plane).

4.2 Model validation for two- and three-phase materials

The sphere-packing algorithm presented in Section 3 has been validated using the electrodes reconstructions of Cell-A and Cell-B. In order to be comparable, the synthetic microstructures have been emulated with the same volume size and spatial resolution than the ones previously considered for the microstructural properties computations (i.e. volumes taken at the same size than the electrode RVE with a voxel discretization of 25 nm).

4.2.1 Validation for the two-phase O_2 electrodes

The reconstructions of the LSCF and LSC O_2 electrodes of Cell-A and Cell-B have been specifically employed for the model validation. The model being built on a stochastic approach, it was preliminary checked that the criterion of repetitiveness is fulfilled when considering the size of synthetic microstructures taken at the electrode RVE (i.e. 9^3 μm^3 for the O_2 electrode). In this condition, it was well verified that two distinct synthetic volumes simulated with the same inputs do not differ from each other in average, in such a way that only one single realization is necessary to draw good statistics on the microstructural properties.

The 3D rendering volumes of the real and synthetic microstructures are compared in Fig. 6a and 6b. As a first approach, the visual inspection of the 3D volumes for both electrodes reveals that the virtual microstructures seem to mimic quite perfectly the real ones. Interestingly, the synthetic solid phase does not present the reminiscence of the initial sphere geometry (as usually observed with typical sphere packing algorithms) but exhibits a more relevant continuous shape. Therefore, it seems that the model would be able to describe accurately the coarse microstructure of Cell-A as well as the finer microstructure of Cell-B.

As illustrated in Fig. 7a and 7b, this first statement is confirmed by the very good agreements between the cumulative solid phase size distributions calculated on the synthetic volumes and the reconstructions. This good agreement is expected as the Weibull distribution for the sphere population in the model was fitted and then shifted (according to Eq. 1 and 5) starting from the LSCF or LSC phase size distribution measured on the reconstruction. Nonetheless, this important result shows that there is a direct relation between the particle size distribution used in the model and the solid

phase PSD in the final microstructure. Therefore, the model is able to generate synthetic volumes that mimic correctly all the length scales of the electrode solid phase. Furthermore, the size distribution of the complementary phase, i.e. porosity, is also well retrieved by the model (Fig. 7a-b). Indeed, a very good agreement is found for both cells, even though a slight discrepancy on the last part of the pore cumulative PSD is detected for the LSCF electrode of Cell-A. This can be explained by some large-scale porosities in the real reconstruction that was not perfectly reproduced by the model.

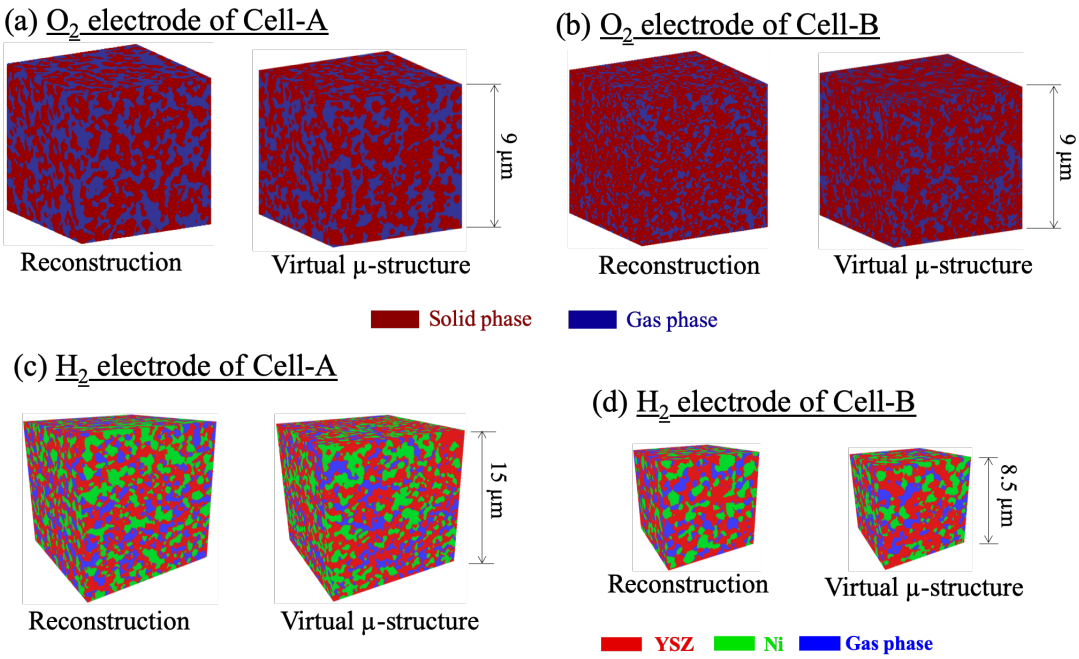

Fig. 6. Visual comparison between the synthetic microstructures and the reconstructed volumes for the O_2 electrodes of (a) Cell-A and (b) Cell-B, and the H_2 electrodes of (c) Cell-A and (d) Cell-B.

To go further in the model validation, the covariance functions and all the electrode morphological and physical parameters of the virtual electrodes have been determined in the same conditions than the data extracted from reconstructions. The comparisons between the real and synthetic electrodes for the covariance function and the microstructural properties are provided in Fig. 7c-d and Table 1, respectively.

As highlighted in Fig. 7c-d for the two cells, a very good agreement between the covariance functions calculated on the real and synthetic electrodes has been found for both solid and gas phases. This first statement is confirmed by the general good consistency regarding the metric properties. Indeed, negligible errors are obtained over the phase volume fractions and the specific surface areas (Table 1), which are directly deduced from the covariance functions [53]. For instance, the disagreement with

respect to the electrode specific surface area, which is a crucial parameter controlling the electrode kinetic rate for the oxygen incorporation [66], does not exceed 4% for both cells. Still on the metric properties, the phase mean diameters are perfectly retrieved by the model as this parameter is directly inferred from the particle size distribution.

A general good agreement is also achieved for the topological properties calculated for both electrodes. Firstly, as observed for the real electrodes, the virtual microstructures are almost fully percolated (more than 99.90% is connected for both solid and pore phases). Secondly, the discrepancy on the geometrical tortuosity and the constrictivity factor remains very limited since the error ranges from 2 to 8%. It can be concluded from this analysis on the metric and topological properties that the proposed particle-based model is able to correctly predict the morphological characteristics of the studied microstructure.

Table 1

Microstructural properties for the O_2 electrodes of Cell-A and Cell-B computed on the tomographic reconstructions and the synthetic volumes.

O_2 electrode of Cell-A													
		Gas phase						**Solid phase (LSCF)**					
Properties	S_p μm^{-1}	δ (%)	ε (%)	$d_p^{(*)}$ (μm)	τ^{geo} (-)	β (-)	M-factor (-)	δ (%)	ε (%)	$d_p^{(*)}$ (μm)	τ^{geo} (-)	β (-)	M-factor (-)
Real μ-structure	3.80	99.96	43.64	0.26	1.22	0.10	0.194	99.99	56.36	0.32	1.34	0.11	0.289
Virtual μ-structure	3.95	99.97	43.71	0.26	1.24	0.11	0.209	99.99	56.29	0.32	1.39	0.12	0.252
Error	+4%	~0%	~0%	~0%	+2%	+5%	+8%	~0%	~0%	~0%	+4%	+8%	-13%
O_2 electrode of Cell-B													
		Gas phase						**Solid phase (LSC)**					
Properties	S_p μm^{-1}	δ (%)	ε (%)	$d_p^{(*)}$ (μm)	τ^{geo} (-)	β (-)	M-factor (-)	δ (%)	ε (%)	d_p (μm)	τ^{geo} (-)	β (-)	M-factor (-)
Real μ-structure	6.28	99.76	28.83	0.12	2.27	0.23	0.078	100	71.17	0.22	1.31	0.31	0.474
Virtual μ-structure	6.09	99.99	28.79	0.12	2.15	0.25	0.082	100	71.21	0.22	1.27	0.32	0.498
Error	-3%	~0%	~0%	~0%	-5%	+8%	+6%	~0%	~0%	~0%	-3%	+5%	+5%

$^{(*)}$ mean phase diameter taken from the PSD.

Regarding the physical properties, the M-factor, which describes the transport phenomena in the solid and pore phases, have been examined. The comparison shows low relative errors that does not exceed +/-13% (Table 1). Indeed, this mismatch combines the errors obtained on all topological properties (the geometrical tortuosity, the constrictivity factor and the phase percolation [7,31]). Nevertheless, considering the general good agreement between the real reconstructions and their digital twins over a large variety of properties, it can be claimed that the model is able to reproduce with a good level of confidence the microstructure of the two O_2 electrodes in LSCF and LSC.

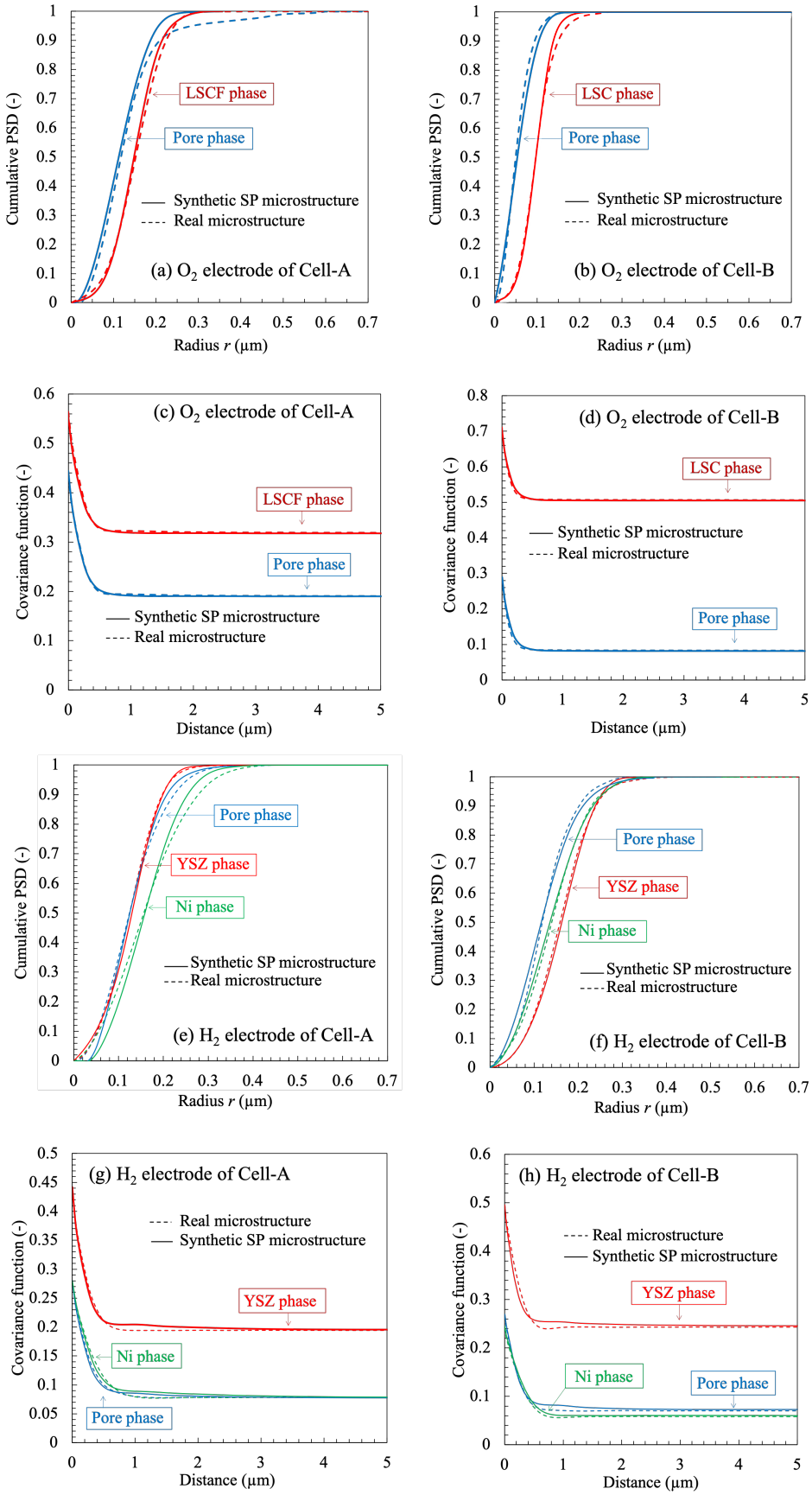

Fig. 7. Comparison between the synthetic and real electrodes microstructures in terms of (a-b,e-f) the cumulative PSDs and (c-d,g-h) the covariance functions for both Cell-A and Cell-B, O_2 and H_2 electrodes.

4.2.2 Validation for the three-phase electrodes

As previously discussed for two-phase electrodes, it has been checked that the generation of one single synthetic volume is sufficient for the cermet of Cell-A when the size is taken at the microstructure RVE of $15^3 \mu m^3$. In the same time for the cermet of Cell-B, the generation of 16 SVEs with a size of 8.5^3 μm^3 was necessary to obtain in average good statistic on the synthetic media (cf. Section 4.1.1).

The 3D rendering volumes of the synthetic microstructures are compared to the Ni-YSZ cermet reconstructions in Fig. 6c-d. As for the LSCF and LSC electrodes, their visual inspection reveals that the more complex microstructure of the three-phase electrodes can accurately be predicted by the model. This preliminary observation is also supported by the good agreement found between the phase size distribution of the real and synthetic microstructures (Fig. 7e and 7f). This good match is obviously obtained for the solid phases, but also on the complementary phase (i.e. porosity) for which the pore size distribution is not directly controlled by the model. This statement means that all the length-scales present in the real reconstructions are accurately taken into consideration by the model, thus proving its relevance.

To check more in depth the model representativeness, the same approach has been adopted for the validation of the two-phase electrodes. Indeed, the covariance functions have been compared in Figs. 7g and 7h and the microstructural properties have been summarized in Tables 2 and 3 for Cell-A and Cell-B respectively. The covariance functions computed for the three phases accurately fit the ones computed on the real reconstructions of both cells. This accordance was confirmed by the good agreement obtained on the metric properties extracted from these curves, namely the phase volume fractions and the specific surface areas. In fact, the errors obtained on these two properties do not exceed +/-4% for the three phases of both cells. This result is of central importance as some kinetic rates (of adsorption/desorption for example) are directly scaled to the electrode specific surface areas [4]. The density of TPBls, which is also a crucial parameter controlling the Ni-YSZ electrode efficiency [9], is well retrieved by the model with negligible relative error that does not exceed +/-6%. Finally, the phase mean diameters were perfectly recovered by the model as expected from the PSD

validation. Consequently, it is found that the metric properties are precisely simulated, providing an initial evidence of the model extension relevance to three-phase materials.

The second step of the validation consists in checking if the topology of the three phases is well reproduced in the simulated electrodes. For this purpose, the synthetic microstructures have been compared in terms of topological properties to the real reconstructions. As a first remark, the three simulated phases are almost totally connected as expected. The average relative error on this parameter is only 2.5%. The highest mismatch is found for the Ni phase of Cell-B for which a connectivity of 98.38% is obtained compared to 92.81% for the real electrode. This slight disagreement seems to be correlated to the rather low Ni volume fraction in Cell-B (i.e. 24.41%). The model ability to predict the geometrical tortuosity and constrictivity factors has also been evaluated. As shown in Tables 2 and 3, these two properties are accurately retrieved for the YSZ backbone of both electrodes, which is the less tortuous and less constrictive phase as it exhibits the highest volume fraction (>44%). For the more constrictive phases (i.e. Ni and porosity), the model succeeds to estimate the geometric tortuosity quite accurately (error < +/-6%); whereas a higher mismatch is obtained on the constrictivity parameter, with a maximum error of +18% obtained for the Ni phase of Cell-A. As a general matter, the model does not perfectly capture the high constrictivities related to geometrical bottlenecks in the real microstructure. This finding is confirmed by the mismatch obtained on the M-factor of these two phases. Indeed, as explained previously, the effective conductivity and diffusivity are directly linked to the topological properties of the medium. A maximum error of +21% is thus detected on the M-factor of the Ni phase of Cell-B (resulting from the accumulation of the morphological errors for this phase).

Table 2
Microstructural properties for the H_2 electrode active layer of Cell-A computed on the tomographic reconstruction and the synthetic volume.

H_2 electrode of Cell-A														
	Gas phase							**Electronic conducting phase (Ni)**						
Properties	S_p (μm^{-1})	δ (%)	ε (%)	d_p (*) (μm)	τ^{geo} (-)	β (-)	M-factor (-)	S_p (μm^{-1})	δ (%)	ε (%)	d_p (*) (μm)	τ^{geo} (-)	β (-)	M-factor (-)
Real μ-structure	2.67	94.74	28.04	0.28	1.67	0.09	0.030	2.30	97.45	27.88	0.33	1.75	0.08	0.041
Virtual μ-structure	2.62	99.51	27.87	0.28	1.62	0.10	0.035	2.25	99.34	28.12	0.33	1.65	0.09	0.049
Error	-2%	+4%	~0%	~0%	-3%	+16%	+17%	-2%	+2%	~0%	~0%	-6%	+18%	+21%
	Ionic conducting phase (YSZ)							**Density of TPBls (Ni/YSZ/gas contact lengths)**						
Properties	S_p (μm^{-1})	δ (%)	ε (%)	d_p (*) (μm)	τ^{geo} (-)	β (-)	M-factor (-)	ξ_{TPBls} (**) (μm^{-2})						
Real μ-structure	3.68	99.78	44.08	0.28	1.43	0.13	0.189	4.78						
Virtual μ-structure	3.83	99.99	44.01	0.28	1.42	0.12	0.193	4.97						
Error	+4%	~0%	~0%	~0%	-1%	-3%	+2%	+4%						

(*) mean phase diameter taken from the PSD. (**) density of 'active' TPBls computed on the connected phases.

Table 3
Microstructural properties for the the H_2 electrode active layer of Cell-B computed on the tomographic reconstruction and the synthetic volume.

H_2 electrode of Cell-B														
	Gas phase							**Electronic conducting phase (Ni)**						
Properties	S_p (μm^{-1})	δ (%)	ε (%)	d_p (*) (μm)	τ^{geo} (-)	β (-)	M-factor (-)	S_p (μm^{-1})	δ (%)	ε (%)	d_p (*) (μm)	τ^{geo} (-)	β (-)	M-factor (-)
Real μ-structure	2.94	94.23	26.55	0.24	1.74	0.39	0.021	2.46	92.81	24.13	0.28	1.81	0.34	0.018
Virtual μ-structure	3.05	99.51	26.16	0.24	1.69	0.43	0.025	2.53	98.38	24.41	0.28	1.76	0.39	0.021
Error	+4%	+4%	~0%	~0%	-3%	+11%	+17%	+3%	+6%	+1%	+1%	-3%	+16%	+18%
	Ionic conducting phase (YSZ)							**Density of TPBls (Ni/YSZ/gas contact lengths)**						
Properties	S_p (μm^{-1})	δ (%)	ε (%)	d_p (*) (μm)	τ^{geo} (-)	β (-)	M-factor (-)	ξ_{TPBls} (**) (μm^{-2})						
Real μ-structure	3.42	99.92	49.55	0.31	1.14	0.44	0.243	6.20						
Virtual μ-structure	3.46	99.99	49.43	0.31	1.13	0.47	0.248	5.83						
Error	+3%	~0%	~0%	+1%	-1%	+8%	+2%	-6%						

(*) mean phase diameter taken from the PSD. (**) density of 'active' TPBls computed on the connected phases.

To sum up, it appears that the model is able to accurately reproduce the metric properties (i.e. volume fractions, specific surface areas, mean phase diameters and density of TPBls), whereas a higher discrepancy on the topological parameters (i.e. constrictivity and tortuosity) is detected for the very high constrictive phases associated with a low volume fraction. Nevertheless, it is worth mentioning that this limitation of the model remains acceptable for the investigated SOCs electrodes (in the worst case, the error on the microstructural factor does not exceed +/-21% for Cell A and +/-18% for Cell-B: cf. Tables 2 and 3). As a consequence, despite the limitation on the

constrictivity factor, it can be concluded that the adapted particle-based model is able to accurately simulate the main electrode properties, and then to provide realistic and representative Ni-YSZ synthetic microstructures.

5 Discussion

5.1 Model advantages and flexibility

With the present validated numerical tool, different synthetic microstructures can be generated by changing the model input parameters. Indeed, the powder mix composition and the particle size distribution as well as the porosity can easily be controlled to generate a large set of different microstructures. This kind of sensitivity analysis can be used to establish the link between the parameters controlling the electrochemical reactions (S_{ij} and TPBl density) to the basic microstructural parameters (composition, porosity and PSD) that are directly controlled by the cell manufacturers [33]. These correlations are of capital importance in a numerical optimization of the electrode microstructures in order to provide practical guidelines for the cell manufacturing.

Aside from the classical electrode microstructure produced by powder processing and sintering, the sphere-packing algorithm can be easily adapted for the generation of alternative and promising electrode architectures. For instance, it is straightforward to introduce some spatial heterogeneities such as agglomerates by controlling the initial sphere allocation. Indeed, as mentioned in Section 3.1, increasing the size of the sub-volumes associated to the number of seeds will introduce some spatial heterogeneities in the final synthetic microstructure. Gradients in composition, particle size or porosities could also be considered by adding a spatial constraint on the volume fractions or particle size distributions. Anisotropies with oriented phases could also be obtained by creating privileged directions when positioning new spheres during the domain filling step (i.e. by using non-uniformly distributed directions in Eq. 3). The spheres could also be changed into needle-like particles or nanofibers for the simulation of original microstructures produced for instance by electrospinning [67].

Finally, it would be very important to address the microstructural modeling for the Ni-YSZ cell support with a bimodal pore size distribution as observed for Cell-B. This substrate holds the thin electrolyte and electrode active layers while promoting the gas diffusion. In that view, the optimization of porosity by virtual material design could be especially relevant. To date, there is no specific geometrical stochastic model available in the literature dedicated to this particular microstructure. For this reason, the sphere-packing model flexibility has been illustrated on this particular case.

5.2 Microstructure modeling for the Ni-YSZ support

The configuration of the model does not allow simulating the microstructure of the Ni-YSZ support of Cell-B. However, thanks to the flexible nature of the proposed particle-based algorithm, it can be easily adapted to take into account the disconnected set of macrospores as observed in Fig. 4. The analysis of the reconstruction in Section 4.1.2 has shown that they are homogeneously distributed within the layer, and have ellipsoid-like morphologies with varying degrees of flattening and tilt.

5.2.1 Model extension to current collecting layer

The sphere-packing algorithm has been modified to simulate the cermet microstructure with a bi-modal pore size distribution. For this purpose, the numerical procedure has been split in three steps detailed hereafter.

(i) A first synthetic microstructure is generated for the percolated micro-pores and solid phases. Since this part of the microstructure results from the partial sintering of the initial powders, the same procedure than the one previously described in Section 3.2 is used.

(ii) The second step of the process is devoted to producing a volume with the disconnected macropores (coming from the use of pore-formers). In this case, a specific algorithm has been developed.

(iii) Finally, the two volumes are merged to model the microstructure with the bi-modal pore size distribution.

For the second step related to the macropore modeling, the same rules than the ones defined for the initial particle positioning in the domain is followed. In this frame, the number of sub-volumes is directly given by the number of macropores. This method

allows generating a uniform but non-periodic repartition of the macro-pores in the volume. Then, the morphology and orientation of these macropores are modelled thanks to parametric ellipsoids with a distribution on size, degree of flattening and orientation. The model input distributions are computed from the real microstructure presented in the previous section. In practice, the ellipsoids are defined in a spherical coordinates system (Fig. 5b) by using three space dimensions a, b, and c; a polar angle θ to describe the volume tilt with respect to the z-axis, and an azimuth angle ϕ to introduce the xy-plane rotation:

$$x = a\cos(\theta)\cos(\Phi) \quad ; \quad y = b\cos(\theta)\sin(\Phi) \quad ; \quad z = c\sin(\theta) \qquad (6)$$

As described in the previous section 4.1.2, the macropores fitting to ellipsoid volumes allowed obtaining the real distribution of the voids dimensions (a, b, and c), and orientation (θ and ϕ).

5.2.2 Elements of model validation

For the simulation of the cell-B Ni-YSZ substrate, a large synthetic volume of 200x200x200 μm^3 was considered to ensure the statistical representativeness of the synthetic structure, and to achieve a good repetitiveness of the model. Thanks to the rather coarse microstructure of the cell support, a resolution of 50 nm has been chosen to generate the synthetic microstructure. Indeed, this voxel size is a good compromise to optimize as far as possible the computation time while keeping a fine description of the microstructure (with this resolution, the rule of 10-15 voxels per particle diameter is still respected).

The visual comparison of one 2D cross-section extracted of the synthetic microstructure and a SEM micrograph of the real electrode is shown in Fig. 8. For what concerns the porosity, it can be seen that the two structures seem to be geometrically similar. In order to validate this preliminary remark, several 36x36x36 μm^3 volumes were cut off the synthetic structure, and their microstructural parameters were averaged. It is worth noting that only 5 SVEs are requested to obtain very good statistics with a negligible standard deviation. From this point of view, the error margins on the data computed on the single volume of 36x36x36 μm^3 can be roughly considered acceptable.

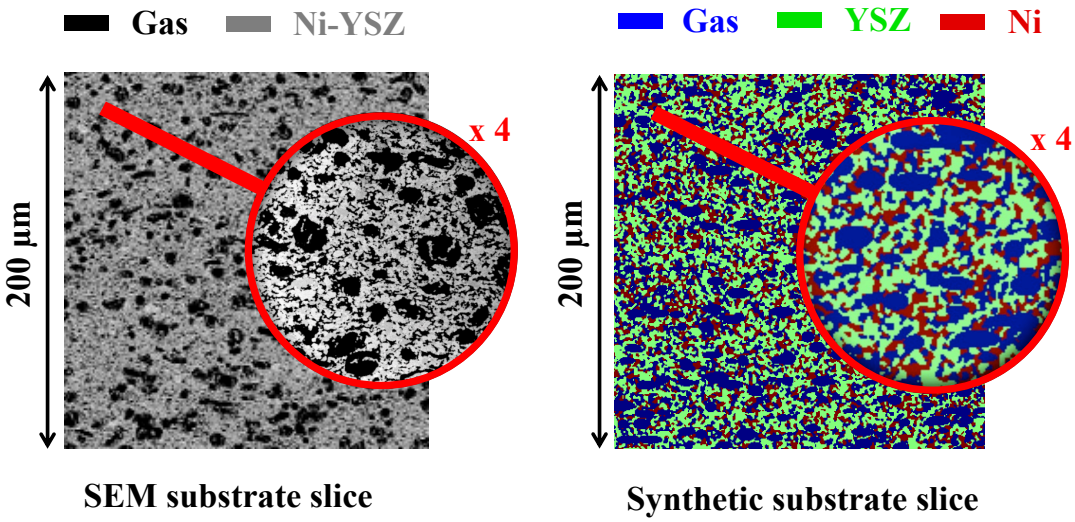

Fig. 8. Comparison of the 2D slice cuts of the real and synthetic microstructures.

The properties computed on the synthetic and real reconstruction are compared in Table 4. It can be noticed that the phase volume fractions were accurately retrieved, as they are input model parameters. Besides, it can be seen that the discrepancies on the properties for the YSZ, Ni and micro-porosity network are rather low. More precisely, the same error bars than the ones obtained for the functional layer were found for the solid phases and the micro-porosity network of the synthetic substrate (Table 4). This statement is rather logical, as the properties of these good percolating phases must not be strongly affected by the presence of the disconnected macrospores. In other words, the properties of the solid and micro-pore phases are mainly controlled by the partial densification of the Ni and YSZ powders while the impact of the pore former is rather limited. For this reason, the following discussion is focused on the parameters directly depending on the macro-porosity distribution (i.e. parameters for the macro-pores and the total pore phase).

As it is used as input model parameter, the macro-pores mean diameter is precisely reproduced in the synthetic microstructure. However, while the specific surface area developed by the micropores network $Sp_{micropores}$ is well simulated (-3% error), the one induced by the macropores $Sp_{macropores}$ is slightly under-estimated (-7% error). This disagreement can be explained by the roughness at the surface of the real macropores that is omitted by the fitted ideal ellipsoids. Regarding the total pore phase, a good agreement was also obtained for the topological properties including the connectivity,

the geometrical tortuosity and the constrictivity factor, for which the errors do not exceed +/-2%, +/-5% and +/-10%, respectively. As discussed previously, the addition of macropores yields a rather low geometrical tortuosity and constrictivity for the gas phase. These specific features of the substrate are well retrieved by the model (Table 4). Therefore, a good agreement is also found for the M-factor of this phase.

Table 4
Microstructural properties for the diffusion layers of the H_2 electrode of Cell-B computed on the tomographic reconstructions. The specific surface area, the connectivity, the volume fraction, the mean particle/pore diameter, the geometrical tortuosity, the constrictivity factor, the M-factor, and the connected TPBl density are given for each electrode phase. It can be noted that the porosity is divided into microporosity and macroporosity

	Cell-B H_2 electrode diffusion layer								
Properties	**S_p**	**δ**	**ε**	**d_p**	**τ^{geo}**	**β**	**M-factor**	**TPBl density**	
Units	**μm^{-1}**	**%**	**%**	**µm**	**-**	**-**	**-**	**μm^{-2}**	
Microporosity	1.92	99.94	31.25	0.61	1.62	0.20	0.131	3.19	**Real**
Macroporosity	0.28		14.21	2.48					
YSZ phase	1.79	99.22	34.85	0.56	1.78	0.43	0.100		
Ni phase	1.25	96.71	19.69	0.42	2.20	0.35	0.011		
Microporosity	1.86	99.97	31.51	0.63	1.57	0.22	0.140	3.08	**Synthetic**
Macroporosity	0.26		13.46	2.42					
YSZ phase	1.81	99.43	34.98	0.56	1.73	0.43	0.110		
Ni phase	1.28	98.46	20.05	0.43	2.08	0.36	0.013		

Moreover, a noticeable anisotropy of the real substrate was detected thanks to the computation of the M-factors in the three spatial directions. It has been found for the synthetic microstructures that the M-factors are respectively 24%, 24% and 33% lower in the z-direction for the YSZ, Ni and pore phases than in the two other directions (compared to 26%, 25% and 36% for the real reconstruction). This quantification shows that the anisotropy is also well captured by the model thanks to the control of the macropores flattening and orientation.

To conclude, the proposed ellipsoid-based model is able to accurately reproduce all the macrospore characteristics of Cell-B substrate. This result can be useful in an objective of microstructural optimization. Indeed, the amount of macro-porosity as well as their morphology and orientation can easily be tuned in the model in order to sweep a wide range of microstructures. The influence of these parameters on the transport properties can thus be investigated in order to limit the diffusional losses across the thick substrate, and hence, enhance the cell performances.

5.3 Model limitations

In order to highlight the limitation and the main drawbacks of this particle-based model, its characteristics in terms of computational time and predictability are compared to a second model based on the multi-Gaussian Random Fields (RF) method. This alternative model, which has already been presented in a previous article [31], is based on radically different assumptions than the proposed Sphere-Packing (SP) model. Indeed, the RF model is founded on the hypothesis that the covariance function can 'fully' characterize the stochastic morphology of the electrode. On the other side, the proposed SP method is an iterative particle-based algorithm that builds a microstructure by positioning representative geometries following a given distribution on size and overlap. It can be inferred that if the RF model considers a statistical representation of the continuous medium as a whole, the SP model breaks it down to a discrete set of representative particles. This later model can thus be considered closer to the classical cell manufacturing process via powders sintering. However, the non-iterative nature of the RF model allows drastically reducing the computational time compared to the common iterative methods. To illustrate this assertion, the time required to emulate the same microstructure of a two-phase electrode with a volume of 9^3 μm^3 and a voxel size of 25 nm has been evaluated by using the two models on the same workstation. It was found that only ≈ 8s is needed to generate the synthetic microstructure by using the RF model, while ≈ 90 minutes is needed for the SP model. This much longer computational time for the iterative SP method constitutes one of the main drawbacks of the method.

Indeed, for a microstructural optimization requiring the generation of a large dataset of microstructures, the method will not be perfectly efficient. From this point of view, it would be interesting to draw a mathematical relation between the targeted volume fraction and the number of particles that could be used to distribute the spheres in one single step, as done with some stochastic geometrical models such as the Boolean model [68-70].

In terms of model predictability to mimic the real electrodes microstructures, it has been found that the morphological properties are generally well retrieved by both RF and SP methods. Indeed, if considering all the tested electrodes, a relative mean error of ≈ 5% and ≈ 4% have been calculated by using the RF and SP microstructures, respectively.

Unfortunately, neither the RF nor the SP models succeeded to perfectly reproduce the very high constrictive phases. In this case, the highest relative errors of 25% and 21% were obtained on the M-factors for the RF and SP microstructures, respectively. This common limitation of the two models seems indicating a change in the geometry and topology of the real phases when approaching the percolation threshold. Since they use the same rules whatever the targeted electrode composition, the two models would thus not be able to catch this morphological evolution across the percolation threshold. Further investigations are thus still necessary to highlight and better analyze this evolution. For example, this expected change in the microstructure geometry could be characterized by reconstructing electrodes below and above the percolation threshold. Nevertheless, in spite of this shortcoming for the high constrictive phases close to the percolation threshold, it is worth underlining that the two models are able to predict the microstructural properties with negligible overall mismatches. Therefore, both models can be used to generate synthetic and representative SOC microstructures.

6 Conclusion

A stochastic geometrical model based on an original sphere-packing method has been developed to produce synthetic microstructures of SOC electrodes. A special attention has been paid to build the model in such a way that the synthetic volumes mimic correctly the complex morphology of the electrodes microstructures. Moreover, the model has been constructed to be able to link the input parameters for the simulations to the powder characteristics used for the cell manufacturing.

The representativeness of the synthetic microstructures has been checked on various FIB-SEM and synchrotron X-ray tomographic reconstructions of typical LSCF, LSC, and Ni-YSZ electrodes. The visual inspection of the electrode reconstructions and their digital twins has revealed that the model is able to reproduce the complex morphology of the tested electrodes. For a full model validation, all the relevant electrode properties have been computed on the real and synthetic volumes. It has been shown that the morphological and physical properties are similar for the synthetic and real media with an average error of ≈4%. The highest discrepancy of ≈21% was found for the constrictivity and M-factor only for the phases close to the percolation threshold. This

discordance has been attributed to some bottleneck effects in the real geometry that are not perfectly captured by the model. Despite this model limitation for the high constrictive phases, the overall good agreement for all the calculated properties means that the synthetic media emulate correctly the complex sintered microstructure of typical LSCF, LSC and Ni-YSZ electrodes.

In order to illustrate the model flexibility to generate a large range of microstructures, the algorithm has been modified to simulate the microstructure of classical Ni-YSZ cell supports exhibiting a bimodal pore size distribution. To validate this adapted version of the model, a typical cell substrate has been specifically reconstructed by synchrotron X-ray holotomography. Thanks to the large reconstructed volume of 36^3 μm^3, the disconnected macro-pores have been separated from the microporosity network and their geometry has been carefully characterized. On the basis of this preliminary image analysis, the model has been validated at the two length scales of the microstructure (i.e. the percolated phases and the macro-pores). It has been shown that the generated synthetic medium mimics all the characteristics of the thick substrate with a high level of confidence.

Acknowledgments

The research leading of these results has received funding from the European Horizon 2020 – Research and Innovation Framework program (H2020-JTI-FCH-2015-1) under grant agreement n°735918 (INSIGHT project) and n°699892 (ECO project). The work has also been partially supported by the French National Agency (ANR) (ECOREVE project). The authors would like to thank Luca Rinaldi for his collaboration in the frame of his master's thesis.

References

[1] W. A. Braff, J. M. Mueller and J. E. Trancik, Nature Climate Change,6 (2016) 964–969.
[2] S.C. Singhal and K. Kendall, "High Temperature Solide Oxide Fuel cells, Fundamental, Design and Applications", Elsevier, 2003.
[3] A. Godula-Jopek, "Hydrogen Production by Electrolysis", Wiley, 2015.
[4] E. Effori, H. Moussaoui, F. Monaco, R. K. Sharma, J. Debayle, Y. Gavet, G. Delette, G. Si Larbi, E. Siebert, J. Vulliet, L. Dessemond, J. Laurencin, Fuel Cells, 19 (2019) 429–444.
[5] Y. Leng, S. H. Chan, Q. Liu, Int. J. of Hydrogen Energy, 33 (2008) 3808-3817.
[6] D. Chen, Z. Lin, H. Zhu, R. J. Kee, J. Power Sources, 191 (2) (2009) 240-252.
[7] L. Holzer, B. Iwanschitz, Th. Hocker, L. Keller, O. Pecho, G. Sartoris, Ph. Gasser, B. Muench, J. Power Sources, 242 (2013) 179-194.
[8] A.V. Virkar, J. Chen, C.W. Tanner, J.-W. Kim, Solid State Ionics, 131 (2000) 189-198.
[9] E. Lay-Grindler, J. Laurencin, G. Delette, J. Aicart, M. Petitjean, L. Dessemond, Int. J. of Hydrogen Energy, 38 (2013) 6917-6929.
[10] A. Bertei, B. Nucci, C. Nicolella, Chemical Engineering Science, 101 (2013) 175-190.
[11] M. Hubert, J. Laurencin, P. Cloetens, J.C. da Silva, F. Lefebvre-Joud, P. Bleuet, A. Nakajo, E. Siebert, Solid State Ionics, 294 (2016) 90-107.
[12] A. Sanson, P. Pinasco, E. Roncari, Journal of European Ceramic Society 28 (2008) 1221-1226.
[13] Y.L. Zhang, S.W. Zha, M.L. Liu, Adv. Mater. 17 (2005) 487.
[14] D. Marrero-López, J.C. Ruiz-Morales, J. Peña-Martínez, J. Canales-Vázquez, P. Núñez, Journal of Solid State Chemistry 181 (2008) 685-692.
[15] F. Monaco, M. Hubert, J. Vulliet, D. Montinaro, J.P. Ouweltjes, P. Cloetens, P. Piccardo, F. Lefebvre-Joud, J. Laurencin, ECS Trans., 91(1) (2019) 653-664.
[16] F. Monaco, M. Hubert, J. Vulliet, J.P. Ouweltjes, D. Montinaro, P. Cloetens, P. Piccardo, F. Lefebvre-Joud, J. Laurencin, J. Electrochem. Soc., 166 (15), (2019) F1229-F1242.
[17] A. Hauch, K. Brodersen, F. Karas, M. Chen, Solid State Ionics, 293 (2016) 27-36.
[18] J.R. Wislon, W. Kobsiriphat, R. Mendoza, H.Y. Chen, J.M. Hiller, D.J. Miller, K. Thorton, P.W. Voorhees, S.B. Adler, S.A. Barnett, Nat. Mater. 5 (2006) 541–544.

[19] N. Vivet, S. Chupin, E. Estrade, T. Piquero, P.L. Pommier, D. Rochais, E. Bruneton, J. Power Sources 196 (2011) 7541–7549.
[20] L. Holzer, B. Münch, B. Iwanschitz, M. Cantoni, T. Graule, J. Power Sources 196 (2011) 7076–7089.
[21] K.N. Grew, Y.S. Chu, J. Yi, A.A. Peracchio, J.R. Izzo, Y. Hwu, F. De Carlo, W.K. Chiu, J. Electrochem. Soc. 157 (6) (2010) B783–B792.
[22] P.R. Shearing, R.S. Bradley, J. Gelb, F. Tariq, P.J. Withers, N.P. Brandon, Solid State Ionics 216 (2012) 69–72.
[23] J.S. Cronin, Y.C.K. Chen-Wiegart, J. Wang, S.A. Barnett, J. Power Sources 233 (2013) 174–179.
[24] M. Stockmar, M. Hubert, M. Dierolf, B. Enders, R. Clare, S. Allner, A. Fehringer, I. Zanette, J. Villanova, J. Laurencin, P. Cloetens, F. Pfeiffer, P. Thibault, Optics Express, 23 (2015) 12720-12731.
[25] S. De Angelis, P. Stanley Jørgensen, V. Esposito, E. Hsiao Rho Tsai, M. Holler, K. Kreka, E. Abdellahi, J. R. Bowen, J. Power Sources, 360 (2017) 520-527.
[26] S. De Angelis, P. Stanley Jørgensen, E. Hsiao Rho Tsai, M. Holler, K. Kreka, J. R. Bowen, J. Power Sources, 383 (2018) 72-79.
[27] M. Hubert, A. Pacureanu, C. Guilloud, Y. Yang, J. C. da Silva, J. Laurencin, F. Lefebvre-Joud, P. Cloetens, Applied Physics Letters, 112 (2018) 203704 1-5.
[28] J. Laurencin, R. Quey, G. Delette, H. Suhonen, P. Cloetens, P. Bleuet, J. Power Sources, 198 (2012) 182-189.
[29] J. Villanova, J. Laurencin, P. Cloetens, P. Bleuet, G. Delette, H. Suhonen, F. UsseglioViretta, J. Power Sources 243 (2013) 841–849.
[30] M. Hubert, Durability of Solid Oxide Cells: an experimental and modelling investigation based on synchrotron X-ray nano-tomography characterization, Thesis of Grenoble University, 2017.
[31] H. Moussaoui, J. Laurencin, Y. Gavet, G. Delette, M. Hubert, P. Cloetes, T. Le Bihan, J. Debayle, Comput. Mater. Sci. 2018, 143, 262.
[32] O. Stenzel, O. Pecho, L. Holzer, M. Neumann, V. Schmidt, AIChE Journal, 63 (2017) 4224-4232
[33] H. Moussaoui, R.K. Sharma, J. Debayle, Y. Gavet, G. Delette, J. Laurencin, J. Power Sources, 412 (2019) 736-748.
[34] H. Moussaoui, J. Laurencin, M. Hubert, R. Sharma, P. Cloetens, G. Delette, Y. Gavet, J. Debayle, ECS Transactions, 91 (1) (2019) 2031-2043.
[35] A.M. Gokhale, S. Zhang, M. Liu, J. Power Sources, 194 (2009) 303-312.
[36] M. Neumann, J. Staněk, O.M. Pecho, L. Holzer, V. Beneš, V. Schmidt, Comput. Mater. Sci., 118 (2016) 353-364.
[37] Y. Zhang, Y. Wang, Y. Wang, F. Chen, C. Xia, J. Power Sources, 196 (2011) 1983-1991.
[38] A. Bertei, C. Nicolella, J. Power Sources, 196 (22) (2011) 9429-9436.
[39] B.S. Prakash, S.S. Kumar, S.T. Aruna, Renew. Sustain. Ener. Rev., 36 (2014)149-179.
[40] H.-W. Choi, D. Gawel, A. Berson, J.G. Pharoah, K. Karan, ECS Trans., 35(1) (2011) 997-1005.
[41] J. Golbert, C.S. Adjiman, N. Brandon, Ind. Eng. Chem. Res., 47 (2008) 7693-7699.

[42] H. Moussaoui, Microstructural optimization of Solid Oxide Cells: a coupled stochastic geometrical and electrochemical modeling approach applied to LSCF-CGO electrode, Thesis of Grenoble University, 2019.
[43] Y. Nishida, S. Itoh, Electrochimica Acta, 56 (2011),2792-2800.
[44] B. Kenney, M. Valdmanis, C. Baker, J.G. Pharoah, K. Karan, J. Power Sources, 189 (2009) 1051-1059.
[45] A. Bertei, H.-W. Choi, J.G. Pharoah, C. Nicolella, Powder Tech., 231 (2012) 44-53.
[46] K. Zheng, M. Ni, Sci. Bull., 61 (1) (2016) 78–85.
[47] C. Metcalfe, O. Kesler, T. Rivard, F. Gitzhofer, N. Abatzoglou, J. Electrochem. Soc., 157(9) (2010) B1326-B1335.
[48] A. Ali, X. Wen, K. Nandakumar, J. Luo, K.T. Chuang, J. Power Sources, 185 (2008) 961-966.
[49] Q. Cai, C.S. Adjiman, N. Brandon, Electrochimica Acta, 56 (2011) 5804-5814.
[50] K. Rhazaoui, Q. Cai, P. Shearing, C.S. Adjiman, N.P. Brandon, ECS Transactions, 35(1) (2011) 1097-1105.
[51] J. Villanova, P. Cloetens, H. Suhonen, J. Laurencin, F. Usseglio-Viretta, E. Lay, G. Delette, P. Bleuet, D. Jauffrès, D. Roussel, A. Z. Lichtner, C. L Martin, Journal of Materials Science 49 (16) (2014) 5626-5634.
[52] F. Usseglio-Viretta, Ph.D. Thesis, Université Grenoble Alpes, Grenoble, France, 2015.
[53] F. Usseglio-Viretta, J. Laurencin, G. Delette, J. Villanova, P. Cloetens, J. Power Sources, 256 (2014) 394-403.
[54] B. Tjaden, D. J. L. Brett, P. R. Shearing, International Materials Reviews, 63 (2) (2018), 47-67.
[55] J. Serra, Image analysis and mathematical morphology: Theoretical advances, Academic Press, Cornell University, 1988.
[56] G. J. Nelson, W. M. Harris, J. J. Lombardo, J. R. Izzo, W. K.S. Chiu, P. Tanasini, M. Cantoni, J. Van herle, C. Comninellis, J. C. Andrews, Y. Liu, P. Pianetta, Y. S. Chu, Electrochemistry Communications, 13 (6) (2011) 586-589.
[57] D. Kanno, N. Shikazono, N. Takagi, K. Matsuzaki, N. Kasagi, Electrochimica Acta, 56 (11) (2011) 4015-4021.
[58] Z. Yan, S. Hara, Y. Kim, N. Shikazono, Int. J. Hydrogen Energy 2017, 42, 30166.
[59] A. Brix, W. S. Kendall, Advances in Applied Probability, 34 (2) (2002) 267-280.
[60] J. Joos, M. Ender, T. Carraro, A. Weber, E. Ivers-Tiffée, "Representative volume element size for accurate solid oxide fuel cell cathode reconstructions from focused ion beam tomography data", Electrochimica Acta 82 (2012) 268-276.
[61] J. Joos, KIT Scientific Publishing, 'Microstructural Characterisation, Modelling and Simulation of Solid Oxide Fuel Cell Cathodes' (2017).
[62] B. A. Horri, C. Selomulya, H. Wang, International Journal of Hydrogen Energy, 37 (20) (2012) 15311-15319.
[63] Y. Petrov, Ellipsoid fit. www.mathworks.com/matlabcentral/fileexchange/24693-ellipsoid-fit, MATLAB Central File Exchange. (accessed February 2020).
[64] M. Noponen, P. Torri, J. Göös, D. Chade, P. Hallanoro, A. Temmo, A. Koit, E. Õunpuu, ECS Transactions, 68 (1) 151-156 (2015).

[65] M. Jabbari, R. Bulatova, A.I.Y. Tok, C.R.H. Bahl, E. Mitsoulis, J.H. Hattel, Materials Science and Engineering: B, 212 (2016) 39-61.
[66] J. Laurencin, M. Hubert, K. Couturier, T. Le Bihan, P. Cloetens, F. Lefebvre-Joud, E. Siebert, Electrochimica Acta, 174 (2015) 1299-1316.
[67] A. Enrico, W. Zhang, M. L. Traulsen, E. M. Sala, P. Costamagna, P. Holtappels, Journal of the European Ceramic Society, 38 (7) (2018) 2677-2686.
[68] C. Lantuéjoul, Geostatistical Simulation, Model and Algorithms, Springer, 2002.
[69] G. Matheron, Random Sets and Integral Geometry, Wiley, New York, 1975.
[70] J. Serra, Comput. Graph. Image Process., 12 (1980) 99-126.

Figure Captions

Fig. 1. SEM cross-section image of Cell-B observed in BSE mode. Higher magnification images reveal the different constitutive cell layers (black color representing porosity, dark grey Ni, and bright grey YSZ).

Fig. 2. Illustration of the different steps for the separation of the macropores from the micropores network. Step *(2)* was not necessary in this particular illustrative case, as the fine micropores were deleted using step *(1)*.

Fig. 3. (a-d) 2D illustration of the three steps for building the particle-based two-phase microstructure; (a) Initial spheres allocation, (b) volume filling (with three examples of spheres overlap extend: high, medium and low in green, black and red respectively), (c) creation of neck curvature, and (d) edge effect correction by volume cropping. (e) Schematic representation of the contact geometry between two particles i and j in the spherical coordinate system, (f) Illustration of the shift between the model input spheres size distribution and the PSD for LSCF computed with the reconstruction for the O_2 electrode of Cell-A.

Fig. 4. (a) Illustration of the macropores separation for the current collector of Cell-B, (b) Pore Size Distribution (PSD) separated in microporosity PSD in blue and macroporosity PSD in red.

Fig. 5. (a) Illustration of a macropore volume fitting with an ellipsoid. (b) Schematic representation of an ellipsoid cut used in the macropores simulation. An illustration is given for the three space lengths a, b and c in a spherical coordinates system where θ is the polar angle (tilt angle with respects to z-axis) and ϕ is the azimuth angle (rotation within the xy-plane).

Fig. 6. Visual comparison between the synthetic microstructures and the reconstructed volumes for the O_2 electrodes of (a) Cell-A and (b) Cell-B, and the H_2 electrodes of (c) Cell-A and (d) Cell-B.

Fig. 7. Comparison between the synthetic and real electrodes microstructures in terms of (a-b,e-f) the cumulative PSDs and (c-d,g-h) the covariance functions for both Cell-A and Cell-B, O_2 and H_2 electrodes.

Fig. 8. Comparison of the 2D slice cuts of the real and synthetic microstructures.

List of Symbols

Roman Symbols:

a, b, and c	Ellipsoid spatial dimensions	µm
d_{ij}	Distance between two overlapping spheres S_i and S_j	µm
d_p	Mean phase diameter	µm
$f_{Weibull}$	Weibull probability density function	–
i $(or\ j)$	Electrode phase: i=ionic (io), electronic (el), porosity (p)	–
k	Shape parameter of the Weibull distribution	–
M_X^x	Microstructure-factor for phase X in the space direction x (equal to the effective/bulk conductivity ratio in direction x)	–
n_{seed}	Number of initial seeds	–
r, r_i, r_j	Sphere radius	µm
S_p	Specific surface area	μm^{-1}
U_i	Sub-volume	μm^3
V	Volume of the domain	μm^3

Greek Symbols:

β	Constrictivity parameter	–
γ_i	Skewness of the PSD_i	–
σ_i	Standard deviation of PSD_i	
ε_X	Phase volume fraction for the phase X	–
ϕ	Azimuth angle	rad
δ_X	Connectivity for the phase X	–
θ	Polar angle	rad
λ	Scale parameter of the Weibull distribution	–
ξ_{TPBs}	Density of triple phase boundary lengths	μm^{-2}
π	Mathematical constant Pi ≈ 3.1416	–
τ_X^{geo}	Geometrical tortuosity for the phase X	–

List of Abbreviations:

FIB-SEM	Focused Ion Beam-Scanning Electron Microscopy
GDC	Gadolinium-Doped Ceria
PSD	Phase Size Distribution
LSC	Lanthanum Strontium Cobaltite
LSCF	Lanthanum Strontium Cobalt Ferrite
MIEC	Mixed Ionic and Electronic Conductor
RF	Random Field
SEM	Scanning Electron Microscopy
SOC	Solid Oxide Cell
SOEC	Solid Oxide Electrolysis Cell
SOFC	Solid Oxide Fuel Cell
SP	Sphere-Packing
SVE	Stochastic Volume Element
RVE	Representative Volume Element
TPBls	Triple Phase Boundary lengths
YSZ	Yttria Stabilized Zirconia